Research Article | Vol. 26, No. 20 | 1 Oct 2018 | OPTICS EXPRESS 26106
Optics EXPRESS

Broadband transmission Raman measurements using a field-widened spatial heterodyne Raman spectrometer with mosaic grating structure

JUN QIU,[1,2,3] XIANGDONG QI,[1,3,4] XIAOTIAN LI,[1,3,*] YUGUO TANG,[1,3] JIRIGA LANTU,[1,3,5] XIAOTAO MI,[1,3] AND HESHIG BAYAN[1,3]

[1]*Changchun Institute of Optics, Fine Mechanics and Physics, Chinese Academy of Sciences, Changchun Jilin 130033, China*
[2]*University of Chinese Academy of Sciences, Beijing 100049, China*
[3]*National Engineering Research Center for Diffraction Gratings Manufacturing and Application, Changchun Jilin 130033, China*
[4]*chinagrating@263.com*
[5]*jiri5998@163.com*
[*]*lixt_1981@163.com*

Abstract: A field-widened spatial heterodyne Raman spectrometer with a mosaic grating structure is developed for the simultaneous sensitivity enhancement and broadband transmission Raman measurements. We optimize the etendue to maximize the signals collected from the samples by using field-widening prisms and employ two mosaic gratings to achieve broadband operation, covering 5638 cm^{-1} with 2.865 cm^{-1} spectral resolution. The signal-to-noise ratios are improved by a factor of more than 11 and show a good stability and fair repeatability. We investigate the effects of the sample thickness and outer layer depth and observe liquids, solids, mixed targets, and anti-Stokes shifts. The instrument exhibits good performance for wide-field, high-resolution broadband transmission Raman measurements.

1. Introduction

Raman spectroscopy is an increasing popular technique in many fields, including physics [1,2], chemistry [3,4], biology [5,6], medicine [7,8], geology [9,10] and semiconductor technology [11,12]. For the instrumental simplicity and ease of use, most Raman spectrometers are designed to observe in a backscatter arrangement. However, in this arrangement, the Raman method is limited to yielding only Raman signals on the surface layers of the sample and leads to errors if Raman signals originating from bulk content of pharmaceutical tablets. Transmission Raman spectroscopy (TRS) is a particularly valuable method for probing the bulk content of diffusely scattering samples, such as turbid or opaque materials because it is rapid, requires no sample preparation, is non-destructive, non-invasive and enables unique molecular identification of bulk components for heterogeneous samples. Its benefits include the removal of the sub-sampling problem from which conventional Raman spectroscopy suffers, and the effective suppression of fluorescence components resulting from coating or capsule layers. Given these advantages, TRS has already been applied in various areas of research, such as biological tissues [13], pharmaceutical qualification and quantification [14,15], and process control applications [16,17].

In the transmission Raman geometry, the laser beam is incident upon one side of the sample and the transmitted Raman light is collected from the opposite side. In this model, the measured Raman signals can be strongly attenuated by a collection aperture, thus resulting in a poor Raman collection efficiency. The lack of signal has hindered the development and application of TRS in various domains. Increasing the collected Raman light throughput is a

#332575 https://doi.org/10.1364/OE.26.026106
Journal © 2018 Received 25 May 2018; revised 23 Aug 2018; accepted 28 Aug 2018; published 21 Sep 2018

Optics EXPRESS

significant challenge for the signal enhancement in TRS measurements by the analyzing spectrometer.

The spatial heterodyne Raman spectrometer (SHRS) has a larger entrance or wider field-of-view (FoV; approximately 100 times) than that of a conventional grating spectrometer of the same resolution. It also has high spectral resolution, a compact and rugged package without moving parts, and is compatible with a pulsed laser and gated detectors under ambient light conditions. All these characteristics together make the SHRS very suitable for large collection areas and ideal for TRS. Strange et al used a non-filed widening SHRS for TRS, the width of the area viewed was found to be seven to nine times that of a dispersive spectrometer, but the signal-to-noise (SNR) was limited by the high levels of background light [18]. Foster et al developed an SHRS that was designed to be fiber coupled for transmission-Raman observations to test paracetamol tablet samples. However, the non-filed widening SHS was limited by the fibre diameter since the larger diameter produces a larger range of angles through the SHS [19]. Field widening is needed to increase the useable field of view without sacrificing the resolving power. This allows larger fibre diameters to be used. The conventional SHRS has the same limiting FoV as that of a Fabry-Perot or traditional Fourier-transform system. Motivated by the fact that an SHRS could be field widened, that an additional 100-fold improvement of the etendue can be achieved by inserting fixed prism in each arm to meet the measurement requirements of a wider area without degrading the spectral resolution. Consequently, the sensitivity of the system will be improved and the area of coverage will be increased. Furthermore, a larger laser spot size or defocused excitation is beneficial to avoid sample photodegradation and thermal degradation.

In a typical SHRS, there is an inverse relationship between the bandpass and spectral resolution, a higher spectral resolution yielding a decrease in the spectral bandpass or vice versa. This relationship makes it difficult to simultaneously satisfy the requirements of broadband pass and high spectral resolution. However, according to the requirements of Raman measurement, it's necessary for the Raman spectrometer to be established to meet the requirements of high spectral resolution and broadband coverage.

In this paper, a new field-widened Mosaic Grating SHRS (MGSHRS) for transmission Raman spectroscopy is described and built, to fully exploit its inherent etendue advantage and achieve a high spectral resolution over a large spectral range. The MGSHRS is based on a Michelson interferometer that is modified by replacing the mirrors in each arm with stationary mosaic gratings and selected prisms are inserted in the configuration of the device, as shown in Fig. 1(a). The alternative mosaic grating is a mosaic of two different groove density gratings that form an equivalent single grating, as shown in Fig. 1(b), and the field-widening prisms are chosen, so that from a geometrical optics point of view the mosaic gratings appear to be normal to the optical axis. In this study, the fundamental principles of a field-widened MGSHRS is provided and the calibration results are given. We compared the field-widened MGSHRS and the MGSHRS with the same instrumental parameters without field widening, the improvement Raman intensity and the improvement SNRs are presented. Some transmission Raman experimental results of targets contained in different plastic tubes and samples of different thicknesses, in a mixture of organic liquids and for inorganic solids, and anti-Stokes shifts are discussed in detail.

2. Theoretical

2.1 Basic theory

The field-widened MGSHRS is depicted in Fig. 1(a). Collimated transmission light enters the MGSHRS and is incident on the beam splitter which transmits and reflects 50% of the incident radiation down the two arms of the interferometer respectively. The light is then incident on the mosaic gratings which are constructed from two adjacent gratings of different groove densities. The gratings are tilted at a fixed angle (the Littrow angle) to the optical axis so that light at the Littrow wavelength exits the interferometer parallel to the optical axis. A

Optics EXPRESS

wavenumber dependent shear is produced between the two beams exiting the interferometer. Light exiting the interferometer is collected with an imaging lens that is designed to image the plane of the grating onto the CCD. In this configuration, a set of overlapping wavenumber dependent Fizeau fringes are imaged onto the detector. Only light at the Littrow wavelength will exit parallel to the optical axis, and the generation of ψ, which is the angle the outgoing wavefronts make with the optical axis, is determined by the grating equation:

$$\sigma(\sin\theta_L + \sin(\theta_L - \psi)) = mG_{1,2}. \tag{1}$$

Where σ is the wavenumber of the incident light, m is the order of diffraction, θ_L is the Littrow angle of the grating, and $G_{1,2}$ are the grating groove densities of the two gratings. For a small γ, the generation of the spatial frequency of fringes is related to the wavenumber by the equation:

$$f_x = 2\sigma\sin\gamma \approx 4(\sigma - \sigma_L)\tan\theta_L. \tag{2}$$

For the axial rays in one dimensional (1-D) SHRS, the input spectral density of $B(\sigma)$ as a function of position x is given by

$$I(x) = \int_0^\infty B(\sigma)\{1 + \cos[2\pi(4(\sigma - \sigma_L)x\tan\theta_L)]\}d\sigma. \tag{3}$$

Where x is measured on the detector in the dispersion plane of the grating. The inverse Fourier transform of the interferogram yielded the transmission Raman spectrum.

The symmetry of the cosine interferogram in Eq. (3) results in folded wavenumbers above and below the Littrow wavenumbers ($\sigma_L \pm \Delta\sigma$.) and the overlapped of anti-Stokes Raman bands and Stokes bands. In our case, the two gratings G_1, G_2 are operated at the 1st diffraction order, and have the same Littrow angle; Vertically tilting one of the mosaic gratings by an angle $\varepsilon/2$, the fringes that are generated by wavenumbers on either side of Littrow are rotated in opposite directions. Therefore, the 2-D FFT of the interferogram in Eq. (4) allows the complete separation of the wavenumbers, and the bandpass of 2-D SHRS is twice that of a 1-D SHRS with the same instrumental parameters [20,21]. The 2-D interferogram can be written as:

$$I(x,y) = \int_0^\infty B(\sigma)\{1 + \cos[2\pi(4(\sigma - \sigma_L)x\tan\theta_L + \sigma y\varepsilon)]\}d\sigma. \tag{4}$$

The maximum theoretical resolving power of the MGSHRS is determined by the mosaic gratings, which is given by:

$$R = \frac{\sigma}{\delta_\sigma} = 4W\sigma\sin\theta_L. \tag{5}$$

Where W is the width of the illuminated diffraction grating; and δ_σ is the spectral resolution.

In the SHRS configuration, the number of pixels on the detector limits the spectral range of a general SHS due to Nyquist sampling theorem. If the detector has N pixels on the x-axis, the spectral range can be expressed as:

$$\Delta\sigma_{1,2} = N\delta_\sigma. \tag{6}$$

From Eqs. (5) and (6), we can see that the spectral resolution is equal to $1/2W\sin\theta_L$, and the spectral range is determined by the number of pixels and the spectral resolution. For Raman measurements which require a large band pass and high resolution, the mosaic grating in our MGSHRS can be chosen with a multiplex of diffraction gratings. If the total number of the different groove density gratings used in one mosaic grating is M ($M \geq 1$) and each spectral range is not overlapped or away from each other, the spectral range can be re-written as [20]:

$$\Delta\sigma_M = MN\delta_\sigma. \tag{7}$$

Optics EXPRESS

From Eqs. (6) and (7), we can see that the MGSHRS can be designed with a spectral range such that the two recovered transmission Raman spectra are adjacent or completely separate, according to the requirements of the Raman measurements. Also, the total spectral range could be improved by increasing the total number of the diffraction gratings contained in one mosaic grating. If M is equal to 2, the Raman photons in one spectral region will be diffracted by only one grating and received by the CCD, but the Raman photons fall on the other grating part will not be received by the CCD. Thus, approximately half of the FoV will be invalid. Increasing the number of mosaic gratings (M>2), the MGSHRS could be an array of SHRS and the FoV of a single field-widened SHRS will be approximately decreased by a factor of M.

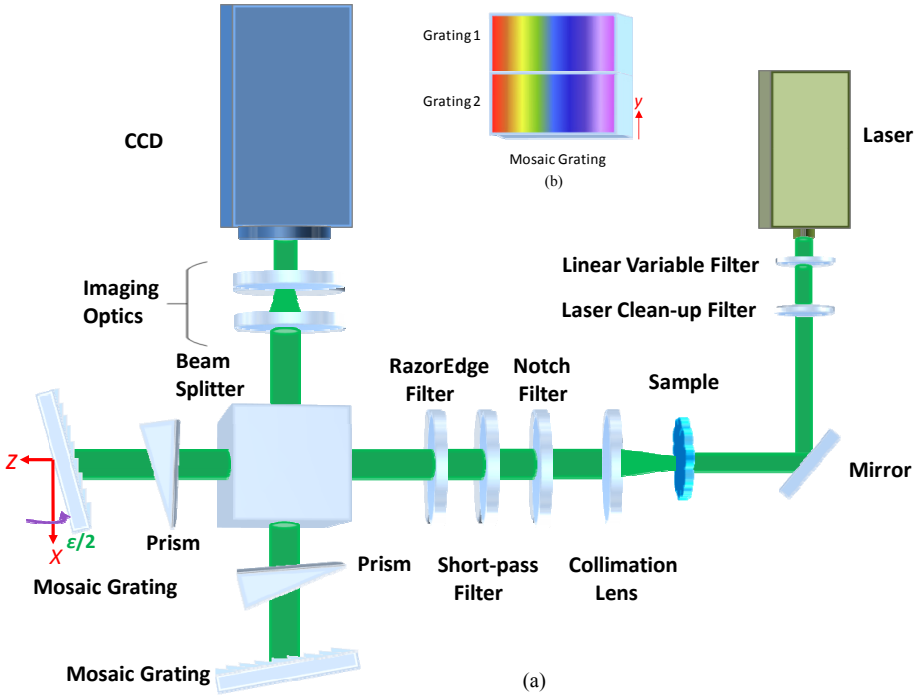

Fig. 1. (a) Spatial heterodyne Raman spectrometer system layout for transmission Raman measurements. (b) Definition of the mosaic grating.

The FoV of the MGSHRS can be greatly increased by using the field widening prisms shown in Fig. 1. In order to field widen the system, selected prisms in the arms of the interferometer are placed appropriately, so the gratings appear normal to the optical axis. The maximum FoV of the field-widened SHRS system can be achieved by minimizing the quadratic dependence of the phase on the incident angle and use of the prism at minimum deviation with angle of incidence γ given by [20]:

$$2(n^2-1)\tan\gamma = n^2\tan\theta_L. \tag{8}$$

Where n is the refractive index of the field widening prisms, and the relationship $n\sin(\alpha/2) = \sin\gamma$ determines the prism apex angle α. Setting the Littrow angle equal to 2.302° and the refractive index is 1.527, the apex angle is calculated to be 2.661°.

For a field-widened MGSHRS, based on the theory of the conventional SHRS system with a shot-noise limit, the SNR can be expressed as [20]:

$$SNR = \sqrt{\frac{\eta A\Omega}{2N} I\delta\sigma T}. \tag{9}$$

Optics EXPRESS

Where η is the optical efficiency, A is the effective area of the system, Ω is the etendue of the system, and I is the intensity of the continuum in photons per second per unit area per steradian per unit wavenumber, which is proportional to the laser power for the measurements. T is the total integration time.

2.2 Calibration theory

The MGSHRS breadboard instrument performance parameters can be estimated by a calibration procedure. This procedure establishes the spectral response of the instrument based on the spatial frequency respond from the known input of a calibration source, such as a mercury lamp [22]. After the fringe frequencies of two known emission lines are measured, the Littrow wavelength of MGSHRS can be acquired by Eq. (10), as follows:

$$\lambda_L = \frac{f_2 - f_1}{(f_2 / \lambda_1) - (f_1 / \lambda_2)}. \tag{10}$$

Where λ_L is the Littrow wavenumber, λ_1 and λ_2 are the known wavelengths from the calibration source, and f_1 and f_2 are the measured fringe frequencies of the two known emission lines. Based on the Eq. (1), the Littrow angle of the diffraction grating is given by Eq. (11):

$$\theta_{L_{1,2}} = arc\sin(\frac{\lambda_L \times G_{1,2}}{2}). \tag{11}$$

According to Eqs. (10) and (11), the width of the grating imaged on the detector can be written as:

$$W = \frac{f_1}{2(1/\lambda_L - 1/\lambda_1)\tan(\theta_L)}. \tag{12}$$

After the grating width is acquired by Eqs. (11) and (12), the total spectral range can be calculated by Eqs. (6) and (7).

3. Experimental

3.1 Breadboard

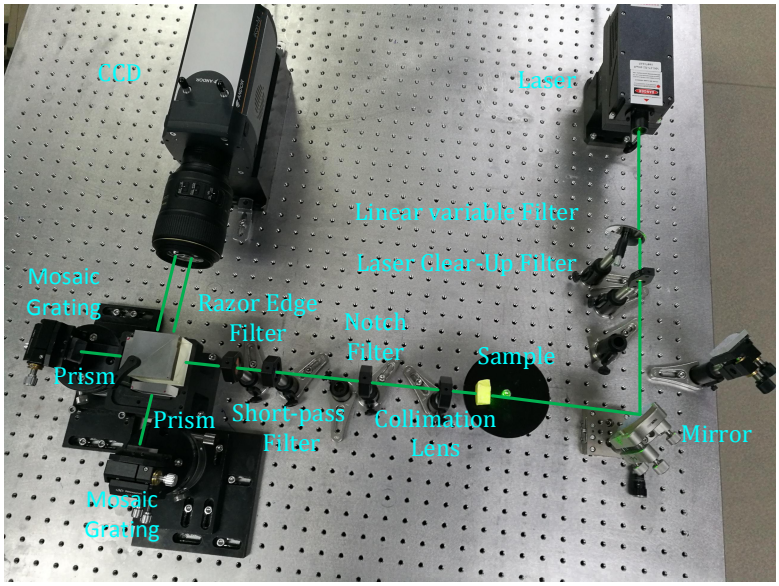

Fig. 2. Layout of spatial heterodyne Raman spectrometer breadboard instrumentation.

Optics EXPRESS

Table 1. Key Parameters of Components Used in the Experimental Breadboard

Components	Parameters	Performance index
Laser	Wavelength	532 nm, CW
	Beam diameter	~2.0 (1/e, mm)
	Beam divergence	<1.5(full angle, mrad)
Grating 1	Groove density	150 gr/mm
	Ruled area	13.1 × 25 mm^2
	Littrow angle	2.302°
Grating 2	Groove density	130 gr/mm
	Ruled area	13.1 × 25 mm^2
	Littrow angle	2.302°
Prisms	Apex angle	2.661°
Beam splitter	Size	50.8 × 50.8 × 50.8 mm^3
CCD	Pixel numbers	1024 × 1024
	Sensor size	13.3 × 13.3 nm^2
	Pixel size	13 × 13 μm^2
Laser clean-up filter	Center wavelength	532 nm
	FWHM Bandwidth	2.0 nm
532 nm long-pass Razor edge Filter	Edge wavelength	536.4 nm
	Transition width	186 cm^{-1}
	Blocking band	OD_{abs}>6@532 nm
532 nm single-notch Filter	Notch band	17 nm
	Blocking band	OD_{abs}>6@532 nm
700 nm Short pass Filter	Cut-off wavelength	700 nm
	Optical density	≥4
Imaging optics	Diameter	62 mm
	Focal length	105 mm

Figure 2 shows the layout of the experimental breadboard. The key parameters of all the commercially-available, off-the-shelf components used in the experiment breadboard are listed in Table 1. The MGSHRS was constructed using a 50.8 × 50.8 × 50.8 mm3 cube beam splitter (model no. 20BC17MB.1, Newport), two prisms where the apex angle was 2.661° (Changchun UP Optotech (Holding) Co., Ltd)), two 150 grooves/mm diffraction gratings and two 130 grooves/mm diffraction gratings (Changchun Institute of Optics, Fine Mechanics and Physics, Chinese Academy of Sciences). The power of the solid state 532-nm green laser could be varied linearly from 0 to 400 mW (Changchun New Industries Optoelectronics Tech. Co., Ltd).

In the experiments, the sample was placed on the focal plane of a 25-mm-diameter collimation lens at a distance of approximately 30 mm. The ambient light and fluorescent light at the wavelengths higher than 700 nm were filtered out using a 700-nm short-pass filter (84-714, Edmund). In some cases, another 532-nm notch filter (NF01-532U-25, Semrock) was used for laser line rejection. A CCD detector with 1024 × 1024 13 μm pixels (iKon-M 934, Andor) was used to record the fringe image. The CCD was cooled to −60°C to reduce the thermal noise within the sensor chip. One mosaic grating was rotated by a small angle about the x-axis. The apex angle of the prism was 2.661°, which was determined by Eq. (8). The flat fielding correction was done in conjunction the calibration process [23] and the Fourier transforms of the fringe images were performed using a 2-D fast Fourier transform (FFT) function. The phase correction method was used for the Fourier-transform spectroscopy [24]. The wavelet threshold de-noising function was then used to effectively separate the signal from the noise [25,26].

3.2 Calibration

From Fig. 3(b) and 3(c), we see that the 576.964 nm line produced 844 fringes, the 579.588 nm line produced 822 fringes and the 668.616 nm produced 161 fringes. Based on Eqs. (10) and (11), the Littrow wavelength was calculated to be 535.587 nm, which corresponded to a grating angle of 2.302°. The width of the grating that was imaged on the detector was estimated to be 21.98 mm, and the spectral resolution was 2.865 cm^{-1}. The spectral range was

Optics EXPRESS

from −1593 cm^{-1} to 4045 cm^{-1} (see Section 4.5). The breadboard experimental results proved that the calibration results were close to the designed MGSHRS performance. The full width at half maximum (FWHM) at 576.964 nm was approximately 3.37 cm^{-1}. This result was in almost exact agreement with the theoretical spectral resolution.

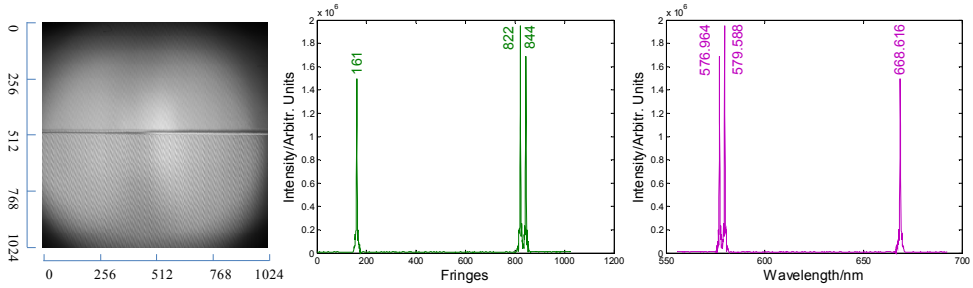

(a) (b) (c)

Fig. 3. (a) Interferogram of the mercury lamp. (b) Spatial frequency profile obtained from the FFT. (c) Mercury lamp spectrum as measured after calibration; the absolute line positions are 576.961 nm, 579.067 nm and 668.617 nm.

4. Results and discussions

4.1 Raman spectral analysis of sulfur and SNR analysis

In Fig. 4(c), the thickness of the sulfur was 4.7 mm, and the recovered Raman spectra of sulfur could be clearly identified. The Raman peaks observed at 153 cm^{-1} and 218 cm^{-1} were assigned to the antisymmetric and symmetric bond-bending modes of the S_8 molecule, respectively. The symmetric bond-stretching mode of sulfur appeared at 473 cm^{-1} and the peak at 85 cm^{-1} was that of the other vibrational mode [27]. There was nearly no difference in the spectral resolution between the two spectra of sulfur.

To quantify the performance of the MGSHRS here, the SNR for the transmission Raman measurements of the spectrum is defined as:

$$SNR = \frac{I_{Peak\_signal}}{RMS_{Noise}}. \tag{13}$$

Comparing the Raman measurement of sulfur with the wide-field measurement of sulfur at the same laser power and same integration time, the intensity of the spectrum was improved by a factor of approximately 3.01. The improvement factor was decreased slightly with an integration times, as shown in Fig. 4(d), which were all nearly 3. The calculated SNRs was also compared, the spectra increased with an integration time and the improvement factor could be more than 11.

As shown in Figs. 5(a) and 5(b), we observed that the SNR plots increased rapidly with the increase of the laser power and the integration time. Then the SNR was slow to change, which was in accordance with Eq. (9). Because all the SNR plots showed the similar tendency as that in Figs. 5(a) and 5(b), which shows a good stability and fair repeatability of the filed-widened MGSHRS.

Where I_{Peak_signal} is the amplitude at the transmission Raman peak and RMS_{Noise} is the root-mean-square (RMS) value of the noise in the spectrum. In our case, the noise was calculated by measuring the RMS in the recovered spectrum of sulfur. Then, the RMS of the noise was divided by the largest amplitude of the 218 cm^{-1} Raman peak, which yielded the measured SNR.

Optics EXPRESS

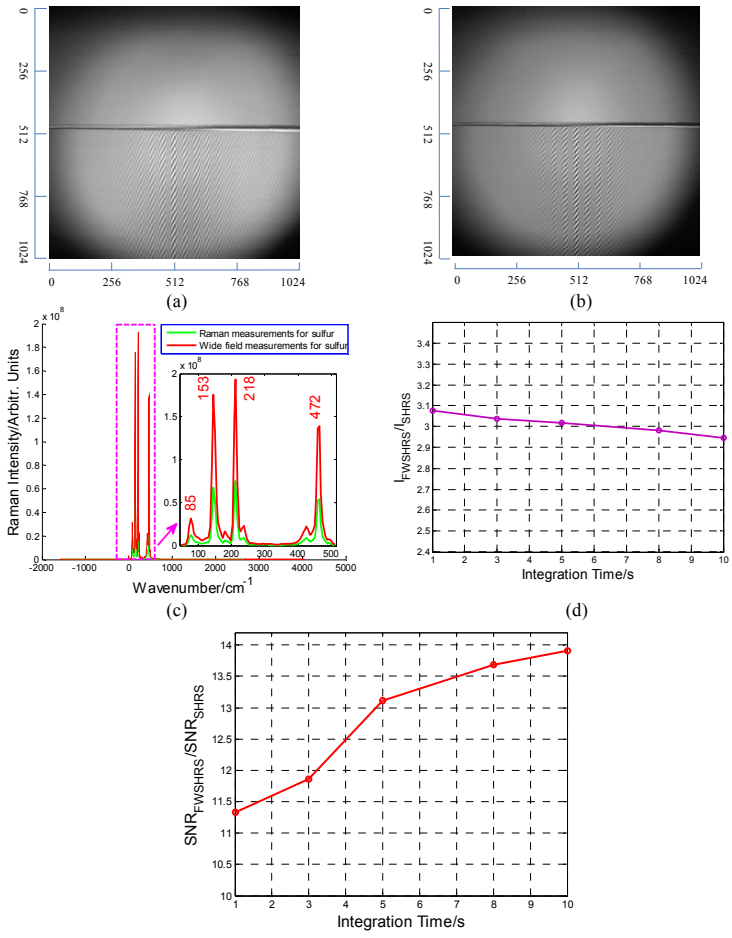

Fig. 4. (a) Interferogram of sulfur at the laser power 50 mW with the integration time 5 s. (b) Interferogram of sulfur at the laser power of 50 mW with an integration time of 5 s without field widening. (c) Recovered Raman measurements and wide-field measurements for sulfur at the laser power of 50 mW with an integration time of 5 s. Plot of the calculated Raman intensities (d) and SNRs (e) for the field-widened MGSHRS and MGSHRS without field widening versus integration times at the laser power of 50 mW.

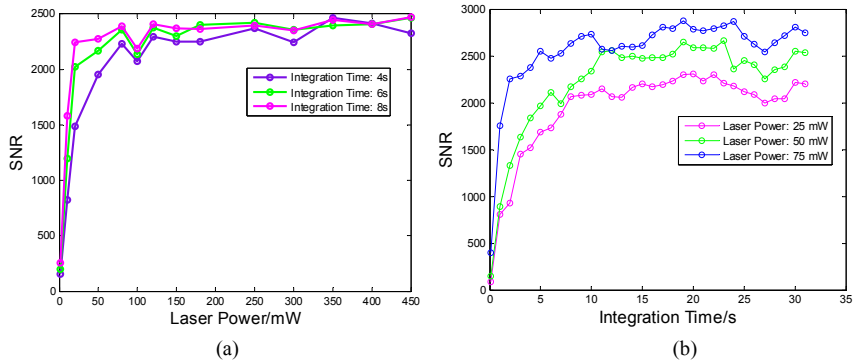

Fig. 5. (a) Measured SNR at different laser powers with integration times of 4 s, 6 s and 8 s. (b) Measured SNR at different integration times at laser powers of 25 mW, 50 mW and 75 mW.

Optics EXPRESS

4.2 Effects of the transmission Raman signal on the sample thickness and outer layer depth

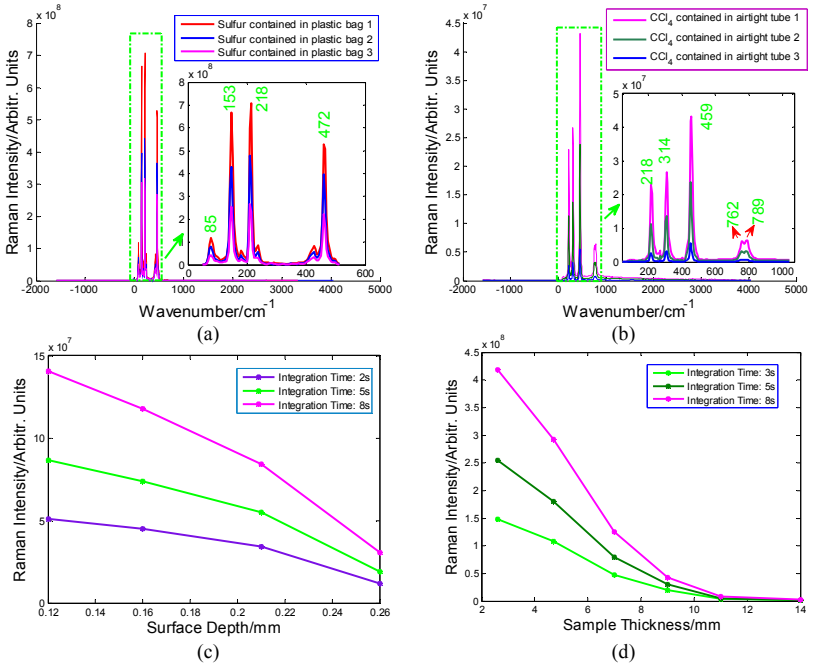

Fig. 6. (a) Recovered Raman spectral of sulfur contained in different-thickness plastic bags at the laser power of 90 mW with an integration time of 8 s. (b) Recovered Raman spectral of CCl_4 contained in different-thickness airtight tubes at the laser power of 60 mW with an integration time of 5 s. (c) Calculated transmission Raman intensities of sulfur versus surface depth at the laser power of 40 mW with integration times of 2 s, 5 s and 8 s. Calculated transmission Raman intensities of sulfur versus sample thickness with a laser power of 70 mW with integration times of 3 s, 5 s and 8 s; the results are presented as linear (d)

In the transmission collection geometry, the laser photons migrated through the sample and produced Raman photons that randomly migrated within the probed medium, which is referred to as Raman photon migration. It is very important to have a good understanding from where the detected Raman photos originated [15]. As the Raman generation is a complex process, a straightforward and simplified way is to investigate the direct dependence of the Raman signal intensity on the thickness of the samples and outer surface layers. Interested in Raman photon migration, we performed a study of the dependence of the Raman intensity on the sample thickness and artificial surface depth.

Under an artificial situation, the transmission Raman of sulfur was measured to investigate the properties and behavior of the generating Raman light in sample contained in artificial outer layers. Figure 6(a) shows the recovered Raman spectra of sulfur contained in plastic bags with different thicknesses at the laser power of 90 mW with integration time of 8 s. The thicknesses of the plastic bags are shown in Table 2 and the main ingredient of the plastic bags was white high density polyethylene. From the Raman spectral of sulfur, all the Raman peaks of sulfur were visible including the weak band at 85 cm^{-1}. In the field-widened MGSHRS system, where lower laser powers or integration times are used, the fluorescence was not observed but the Raman signals were apparently affected by the plastic bags. The data in Fig. 6(c) shows that the collection of Raman signals gradually decreased with the increasing thickness of the plastic bags and at a depth of 0.21 mm the Raman signals originating from the sulfur were reduced by approximately three times of two-thirds from

Optics EXPRESS

their original levels at a depth of 0.12 mm. However, the Raman spectra regarding the outer layer at the front and back of the sample were obtained.

Figure 6(b) shows the recovered Raman spectra of CCl_4 contained in airtight tubes with different thicknesses (see Table 2) at the laser power of 60 mW with an integration time of 5 s. The low energy band at 218 cm^{-1} was attributed to the bending mode of *E* symmetry. The degenerate deformation (T_2) and the symmetric stretching vibrational modes (A_1) were clearly visible at 314 cm^{-1} and 459 cm^{-1}, respectively. The fourth band at 762 cm^{-1} was assigned to the combination mode $T_2 + A_1$. The fifth band at 790 cm^{-1} was assigned to the mode T_1 [28]. There was almost no spectral resolution difference among the three spectra. Owing to the field-widened transmission system, lower laser powers or shorter integration times were required, so fluorescence that may hamper the spectra by causing fluctuations in the spectral baseline was not observed in the experiments. However, obviously, the SNR was lower because thicker tubes were used.

Figure 6(d) show the collected Raman signals of sulfur with different thicknesses presented as linear. The thicknesses of the sulfur were 2.6 mm, 4.7 mm, 7.0 mm, 9.0 mm, 11.0 mm and 14.0 mm. The positioning of the 2.6 mm lump of sulfur from the surface to a depth of 14.0 mm reduced its intensity substantially. Therefore, the field-widened MGSHRS for transmission measurements exhibited a dependence of the Raman signals on the thickness of the sample. This is because the field-widened system is very sensitive to a change of the Raman photons. The extra thickness of the sample made it difficult for the probe photons migrate through the sample, thus its own Raman signal was lost at the entrance of the detection system.

For transmission Raman measurements, the field-widened MGSHRS system revealed that the increase of the sample thickness or outer layer resulted in a decrease of the Raman signal detected. On the other hand, the results were able to reveal the presence of inner-sample irrespective of whether it contained in an “impurity” in the outer layer or the high sensitivity of the field-widened MGSHRS system to detect changes of Raman photons caused by the sample thickness without the loss of spectral resolution.

Table 2. Plastic Bags and Airtight Tubes Used in the Experiment

Artificial outer layer	Bag 1	Bag 2	Bag 3	Tube 1	Tube 2	Tube 3
Thickness/mm	0.12	0.16	0.21	0.50	0.80	1.10

4.3 Spectral analysis of solid sodium sulfate (Na_2SO_4) and potassium sulfate (K_2SO_4)

According to the T_d symmetry of the free anion SO_4^{2-}, the $v_1(A_1)$ is the symmetric stretching mode, the $v_2(E)$ and $v_4(F_2)$ modes correspond to the bending vibration, and the $v_3(F_2)$ is an anti-symmetric stretching mode. Figure 7(a) shows the recovered Raman spectrum of solid sodium sulfate at the laser power 75 mW with the integration time 5s. The main Raman peak at 992 cm^{-1} was assigned to the $v_1(A_1)$ mode. The v_2 and v_4 modes were detected in the low wavenumber region and the v_3 mode was in the high wavenumber region. For a clearer observation in the spectrum, the Raman spectra in the range of 370 cm^{-1} to 710 cm^{-1} and 1080 cm^{-1} to 1190 cm^{-1} were represented on an enlarged scale. The weak Raman peaks of Na_2SO_4, which corresponded to the v_2, v_3, v_4 mode could be clearly seen in the spectrum [29]. Figure 7(b) shows the recovered Raman spectrum of solid potassium sulfate at the laser power of 75 mW with an integration time of 5s. The $v_1(A_1)$ vibration band centered at 983 cm^{-1} was specific to the sulfate anion. The v_2 mode appeared at approximately 449 cm^{-1}, the v_4 mode was centered at about 616 cm^{-1}, and the triplet v_3 occurred between 1107 cm^{-1} and 1145 cm^{-1}. The detection capabilities of the field-widened MGSHRS demonstrated in this work are very promising for applications in geochemistry and environmental measurements.

Optics EXPRESS

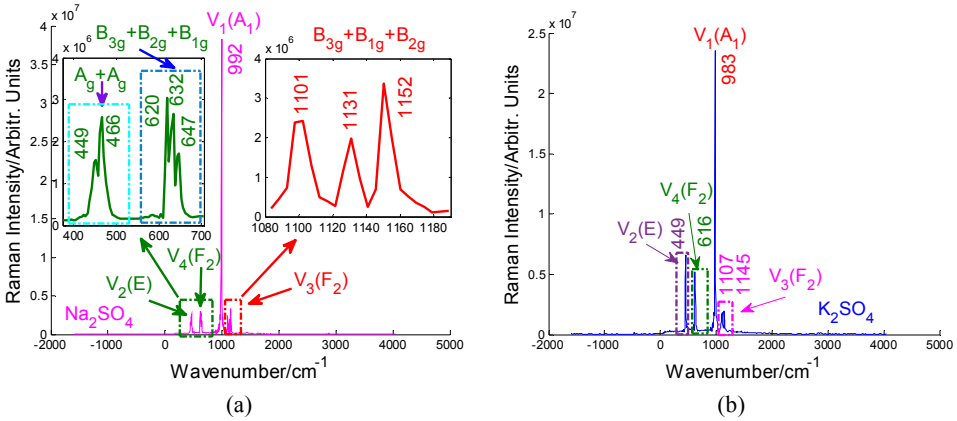

Fig. 7. Recovered Raman spectra of solid sodium (a) and potassium sulfates (b) at the laser power 75 mW with the integration time 5 s.

4.4 Raman spectra analysis of a mixture of inorganic solids and organic liquids

Figure 8(a) shows the Raman spectra of sulfur, titanium dioxide, potassium sulfate and a mixture of the three inorganic solids. In the Raman spectra of sulfur and potassium sulfate, the Raman peaks mentioned above were clearly visible. In the transmission Raman spectra of the titanium dioxide, the strong and sharp band at 143 cm^{-1} was assigned to the E_g mode. The weak bands at 396 cm^{-1} and 639 cm^{-1} arose from the B_{1g} mode. The weak peak at 516 cm^{-1} was attributed to the A_{1g} and B_{1g} modes. The mixing mass ratio of the mixture was 2:2:1. The main Raman peaks at 153 cm^{-1}, 218 cm^{-1} and 472 cm^{-1} of the sulfur, the main peak at 143 cm^{-1} of titanium dioxide and the main peak at 983 cm^{-1} of potassium sulfate were well visualized in the Raman spectrum of the mixture of the three solids. The weak peak at 85 cm^{-1} of sulfur, the weak peaks at 516 cm^{-1} and 639 cm^{-1} of titanium dioxide and the weak peak at 449 cm^{-1} of potassium sulfate were also observed in the Raman spectrum of the compounds.

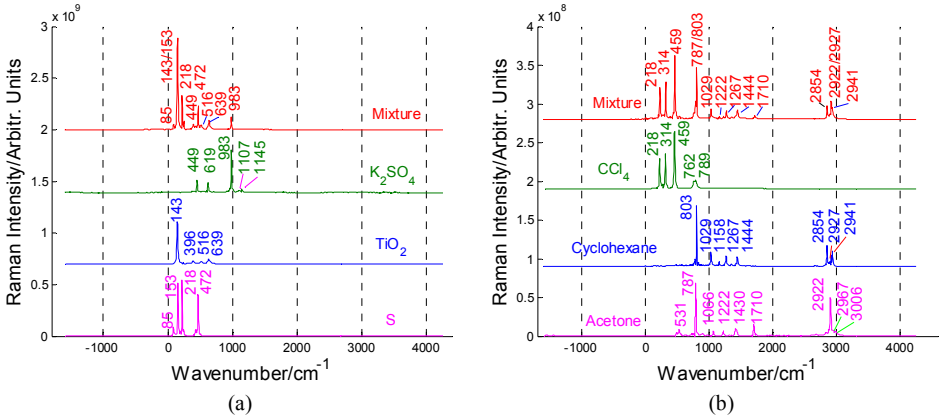

Fig. 8. (a) Recovered Raman spectra of inorganic solids at the laser power of 60 mW with an integration time of 15 s. (b) Recovered Raman spectra of organic liquids at the laser power of 90 mW with an integration time of 10 s.

Figure 8(b) shows the Raman spectra of acetone, cyclohexane, carbon tetrachloride and a mixture of the three organic liquids. In the spectra of acetone, cyclohexane and carbon tetrachloride, the main Raman peaks were well detected. The mixing volume ratio of the

Optics EXPRESS

mixture was 2:1:1. Because of the different intensities of the three organic liquids, the 531 cm^{-1}, 787 cm^{-1}, 1222 cm^{-1}, 1710 cm^{-1}, and 2922 cm^{-1} peaks of acetone, the 803 cm^{-1}, 1029 cm^{-1}, 1267 cm^{-1}, 1444 cm^{-1}, 2854 cm^{-1}, 2927 cm^{-1} and 2941 cm^{-1} peaks of cyclohexane, and the 218 cm^{-1}, 314 cm^{-1}, 459 cm^{-1} and 789 cm^{-1} peaks of carbon tetrachloride could be distinguished in the Raman spectrum of the mixture of the three organic liquids.

Under the complex condition, the field-widened MGSHRS has the ability to identify the mixtures with rapid analysis and response, though the spectrum of the mixture contained more information than the pure analytes. The results demonstrate that the field-widened MGSHRS has a high instrumental sensitivity to distinguish the weak Raman signals in the spectrum of the mixture and a broad spectral range to meet the requirements of the Raman detection. If a wider spectral coverage and high resolution of MGSHRS are needed for the Raman detection, additional different groove density gratings can be mosaicked in the mosaic grating. we also proved that the instrument is capable of identifying the potential interferences by non-target compounds or contaminants under certain conditions.

4.5 Stokes and anti-Stokes Raman detection of carbon tetrachloride and sulfur

Figure 9 shows the Stokes and anti-Stokes Raman spectra of carbon tetrachloride (a) and sulfur (b) that were recorded at room temperature. To test the anti-Stokes band, the edge filter was replaced with a 532-nm notch filter to limit the pass band. In the Stokes region (green spectra) and anti-Stokes region (purple spectra), the Raman shifts at 472 cm^{-1} for sulfur and at 459 cm^{-1} and 762/789 cm^{-1} for CCl_4 could be clearly identified without overlap. The 58 cm $^{-1}$,153 cm^{-1} and 218 cm $^{-1}$ bands of sulfur and the 218 cm^{-1} and 314 cm $^{-1}$ bands of CCl_4 were filtered by the notch filter. The green spectrum and purple spectrum diffracted by grating 1, and its spectral range was estimated to be −1593 cm^{-1} to 1535 cm^{-1}. The blue spectrum diffracted by grating 2, and its spectral rang was estimated to be 917 cm^{-1} to 4045 cm^{-1}. Thus, the total spectral range was extended to 5638 cm^{-1}.

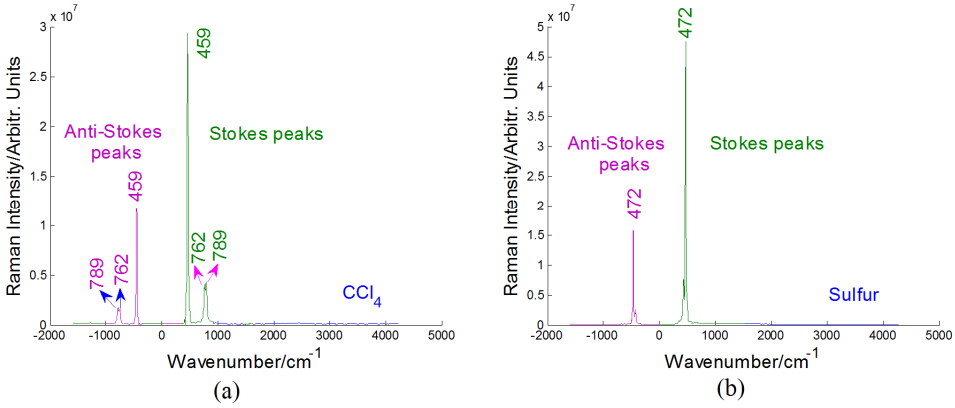

Fig. 9. (a) Stokes and anti-Stokes Raman spectra of carbon tetrachloride at the laser power of 60 mW with an integration time of 5 s. (b) Stokes and anti-Stokes Raman spectra of sulfur at the laser power of 80 mW with an integration time of 4 s.

5. Summary

We have proposed a field-widened MGSHRS breadboard for broadband transmission Raman measurements. The new MGSHRS has been constructed with two fixed field-widening prism (apex angle: 2.661°) placed in the arms of the interferometer and a mosaic grating consisting of a 130 gr/mm grating and a 150 gr/mm grating. The system performance and in particular enhancement effect have been demonstrated in the transmission collection system.

Optics EXPRESS

In the experiments, the Raman spectra of sulfur detected by the field-widened MGSHRS and a MGSHRS with the same instrumental parameters without field widening were compared. The transmission Raman signals can be enhanced by a factor of 3 without the loss of spectral resolution and SNRs can be improved more than 11 times. The current optical properties of the optics may limit the enhancement factor. We propose the enhancement sensitivity factor can be further improved by coated prisms or a larger aperture of optics. We demonstrated the field-widened MGSHRS exhibits a good stability and fair repeatability by measuring the SNR with different integration times and laser powers, and the SNR can reach approximately 3000 at a low laser power 75 mW with a short integration time 10 s. The field-widened MGSHRS has an enhanced detection capability owing to factors such as high sensitivity, fast response time, low laser power requirements, good stability and fair repeatability, and all these advantages allow specifically for transmission Raman spectroscopy.

Under the artificial condition, we performed a study of the Raman intensity on sample thickness and outer layer depth that have direct effects of the Raman photon migration in the transmission geometry. The results show that the Raman signal originates from the sample, irrespective of whether it is coated by different plastic bags or different tubes. Raman signals measured by the transmission Raman collection system largely depend on the thickness of the sample and outer layer depth largely. On the other hand, the consequence of these results shows that the sensitivity of the spectrometer is very high so that the changes of the transmission Raman photons caused by the sample thickness can be detected without the loss of spectral resolution and fluorescence was not observed. This analysis provides great insight for the quality control in a pharmaceutical application.

Furthermore, we demonstrate that the spectrometer has not only a high instrument sensitivity, which is able to separate targeted compounds by testing a mixture of organic liquids or inorganic solids, but also has a broad spectral range. The results show that the field-widened MGSHRS can easily meet the Raman requirements for identifying potential interferences by non-target compounds or contaminants under an intended condition. Finally, the anti-Stokes bands of sulfur and carbon tetrachloride were observed.

The wide-field and broadband transmission Raman detections do not require long integration times or high laser powers, do not include a loss of sensitivity or spectral resolution, and the transmission Raman signals and SNRs can be greatly enhanced by a larger collection FoV. The system provides significant advantages to match the needs of transmission Raman spectroscopy and is therefore very promising for a given application.

Funding

National Natural Science Foundation of China (NSFC) (61505204); Jilin Province Science & Technology Development Program Project in China (20170520167JH); Chinese Ministry of National Science and Technology (2014CB049500); National R & D Projects for Key Scientific Instrument Project (ZDYZ2008-1); National Major Scientific Instrument and Equipment Development Projects (2014YQ120351).

References

1. H. Lin, C. S. Liao, P. Wang, and J. X. Cheng, "Spectroscopic stimulated Raman scattering imaging of highly dynamic specimens through matrix completion," Light Sci. Appl. **7**(5), 17179 (2018).
2. P. Lutsyk, R. Arif, J. Huby, A. Bukivskyi, O. Vinijchuk, M. Shandura, V. Yakubovskyi, Y. Kovtun, and G. A. Rance, "A sensing mechanism for the detection of carbon nanotubes using selective photoluminescent probes based on ionic complexes with organic dyes," Light Sci. Appl. 5(2), e16028 (2016).
3. L. S. Fan, L. Constanin, D. W. Li, L. liu, K. Keramatnejad, C. Azina, X. Huang, H. R. Golgir, Y. Lu, Z. Ahmadi, F. Wang, J. Shield, B. Cui, J. F. Silvain, and Y. F. Lu, "Ultraviolet laser photolysis of hydrocarbons for nondiamond carbon suppression in chemical vapor deposition of diamond films," Light Sci. Appl. 7(4), 17177 (2018).
4. M. Sun, Z. Zhang, P. Wang, Q. Li, F. Ma, and H. Xu, "Remotely excited Raman optical activity using chiral plasmon propagation in Ag nanowires," Light Sci. Appl. **2**(11), e112 (2013).

Optics EXPRESS

5. A. M. Christine, D. B. France, C. R. Thomas, Doney, and O. Madden, "Ft-Raman Spectroscopy as a Method for Screening Collagen Diagenesis in Bone," J. Archaeol. Sci. **42**, 346–355 (2014).
6. S. Mattana, M. Mattarelli, L. Urbanelli, S. Krizia, E. Carla, D. S. Mauro, F. Daniele, and C. Silvia, "Non-contact mechanical and chemical analysis of single living cells by microspectroscopic techniques," Light Sci. Appl. **7**(2), 17139 (2018).
7. H. Wang, M. A. Boraey, L. Williams, D. Lechuga-Ballesteros, and R. Vehring, "Low-frequency Shift Dispersive Raman Spectroscopy for the Analysis of Respirable Dosage Forms," Int. J. Pharm. **469**(1), 197–205 (2014).
8. J. Bonefacino, H.-Y. Tam, T. S. Glen, X. Cheng, C.-F. J. Pun, J. Wang, P.-H. Lee, M.-L. V. Tse, and S. T. Boles, "Ultra-fast polymer optical fiber Bragg grating inscription for medical devices," Light Sci. Appl. **7**, 17161 (2018).
9. A. K. Misra, S. K. Sharma, C. H. Chio, P. G. Lucey, and B. Lienert, "Pulsed remote Raman system for daytime measurements of mineral spectra," Spectrochim. Acta A Mol. Biomol. Spectrosc. **61**(10), 2281–2287 (2005).
10. J. D. Stopar, P. G. Lucey, S. K. Sharma, A. K. Misra, G. J. Taylor, and H. W. Hubble, "Raman Efficiencies of Natural Rocks and Minerals: Performance of a Remote Raman System for Planetary Exploration at a Distance of 10 Meters," Spectrochim. Acta A Mol. Biomol. Spectrosc. **61**(10), 2315–2323 (2005).
11. B. Fazio, P. Artoni, M. A. Iatì, C. D. Andrea, M. J. Lo Faro, S. D. Sorbo, S. Pirotta, P. G. Gucciardi, P. Musumeci, C. S. E. Vasi, R. Saija, M. Galli, F. Priolo, and A. Irrera, "Strongly Enhanced Light Trapping in a Two-Dimensional Silicon Nanowire Random Fractal Array," Light Sci. Appl. **5**(4), e16062 (2016).
12. C. Hu, Q. Chen, F. Chen, T. H. Gfroerer, M. W. Wanlass, and Y. Zhang, "Overcoming diffusion-related limitations in semiconductor defect imaging with phonon-plasmon-coupled mode Raman scatrtering," Light Sci. Appl. **7**(1), 23 (2018).
13. N. Stone and P. Matousek, "Advanced Transmission Raman Spectroscopy: A Promising Tool for Breast Disease Diagnosis," Cancer Res. **68**(11), 4424–4430 (2008).
14. C. Eliasson, N. A. Macleod, L. C. Jayes, F. C. Clarke, S. V. Hammond, M. R. Smith, and P. Matousek, "Non-invasive quantitative assessment of the content of pharmaceutical capsules using transmission Raman spectroscopy," J. Pharm. Biomed. Anal. **47**(2), 221–229 (2008).
15. P. Matousek and A. W. Parker, "Bulk Raman analysis of pharmaceutical tablets," Appl. Spectrosc. **60**(12), 1353–1357 (2006).
16. N. A. Macleod and P. Matousek, "Emerging non-invasive Raman methods in process control and forensic applications," Pharm. Res. **25**(10), 2205–2215 (2008).
17. N. Everall, I. Priestnall, P. Dallin, J. Andrews, I. Lewis, K. Davis, H. Owen, and M. W. George, "Measurement of spatial resolution and sensitivity in transmission and backscattering Raman spectroscopy of opaque samples: impact on pharmaceutical quality control and Raman tomography," Appl. Spectrosc. **64**(5), 476–484 (2010).
18. K. A. Strange, K. C. Paul, and S. M. Angel, "Transmission Raman Measurements Using a Spatial Heterodyne Raman Spectrometer (SHRS)," Appl. Spectrosc. **71**(2), 250–257 (2017).
19. M. J. Foster, J. Storey, and M. A. Zentile, "Spatial-heterodyne spectrometer for transmission-Raman observations," Opt. Express **25**(2), 1598–1604 (2017).
20. J. M. Harlander, "Spatial heterodyne spectroscopy: interferometric performance at any wavelength without scanning," Thesis (Ph.D.) University of Wisconsin—Madison (1991), Chap. 3, Chap. 5.
21. T. Nathaniel, "Spatial Heterodyne Raman Spectroscopy," University of Surrey (2011), Chap. 4.
22. C. R. Englert, J. M. Harlander, J. C. Owrutsky, and J. T. Bays, "Shim-Free Breadboard Instrument Design, Integration, and First Measurements," NRL/MR/7640–05–8926, 1 (2005).
23. C. R. Englert and J. M. Harlander, "Flatfielding in spatial heterodyne spectroscopy," Appl. Opt. **45**(19), 4583–4590 (2006).
24. C. R. Englert, J. M. Harlander, J. G. Cardon, and F. L. Roesler, "Correction of phase distortion in spatial heterodyne spectroscopy," Appl. Opt. **43**(36), 6680–6687 (2004).
25. M. Misiti, Y. Misiti, G. Oppenheim, and J. M. Poggi, *Wavelet Toolbox User's Guide* (The Math Works, Inc, 2018).
26. J. Qiu, X. Qi, X. Li, Z. Ma, Y. Jirigalantu, X. Tang, X. Mi, R. Zheng, Zhang, and Bayanheshig, "Development of a spatial heterodyne Raman spectrometer with echelle-mirror structure," Opt. Express **26**(9), 11994–12006 (2018).
27. J. Lin and Y. Q. Li, "Ultralow frequency Stokes and anti-Stokes Raman spectroscopy of single living cells and microparticles using a hot rubidium vapor filter," Opt. Lett. **39**(1), 108–110 (2014).
28. D. Tuschel, "Practical Group Theory and Raman Spectroscopy, Part II: Application of Polarization," Spectrosc. **29**, 15 (2014).
29. B. M. Kawther, H. K. Thomas, A. Hassen, and D. F. Marc, "Raman study of cation effect on sulfate vibration modes in solid state and in aqueous solutions," J. Raman Spectrosc. **44**(11), 1603–1608 (2013).